Chapter 4

Optical Scanning Holography: Applications

So far, the applications of optical scanning holography span over five diverse areas: scanning holographic microscopy [(Poon, Doh, Schilling, Wu, Shinoda, and Suzuki (1995)], 3-D image recognition [(Poon and Kim (1999)], 3-D optical remote sensing [Kim and Poon (1999)], 3-D holographic TV and 3-D display [Poon (2002a)], and 3-D cryptography [Poon, Kim, and Doh (2003)]. In this chapter, we will only cover three areas of the applications mentioned above. We will focus on scanning holographic microscopy, 3-D holographic TV and 3-D display, and 3-D cryptography in that order, as the other areas have been recently reviewed in the book chapters [Poon (2002b), Poon (2005)].

4.1 Scanning Holographic Microscopy

Three-dimensional (3-D) imaging is a formidable task for optical microscopy as it is well known that the greater the *lateral resolution* Δr is, the shorter the *depth of focus* Δz will be. In other words, if we want to create a higher lateral resolution in the microscopic imaging system, say by using a high *numerical aperture* (NA) lens, we will have to compromise the system with a shorter depth of focus where only a thin section of the specimen can be imaged. To demonstrate this fact, a simple quantum mechanical argument is convenient to use here.
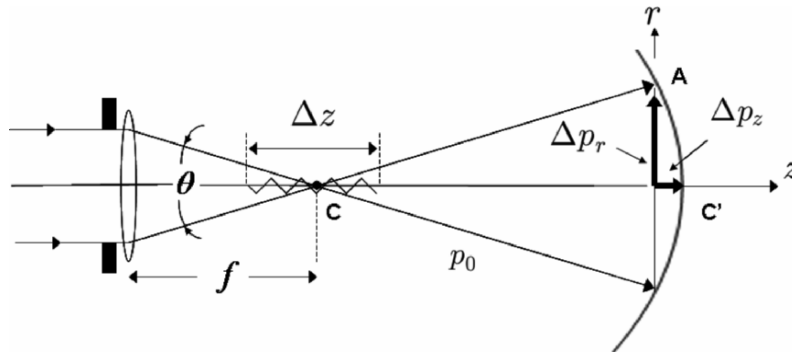

Fig. 4.1 Uncertainty principle used to find resolution and depth of focus.

Let us first find the lateral resolution, Δr. Quantum mechanics relates the minimum uncertainty in a position of quantum, Δr, to the uncertainty of its momentum, Δp_r, according to the relationship

$$\Delta r \Delta p_r \geq h, \tag{4.1-1}$$

where Δp_r is the momentum difference between rays CA and CC′ along the r-direction, i.e., the transverse direction as shown in Fig. 4.1, where parallel rays are focused by a lens. Now the momentum of the CA ray and the CC′ ray is $p_0 \sin(\theta/2)$ and zero along the r-direction, respectively, where $p_0 = h/\lambda_0$ is the momentum of the quantum. Hence, $\Delta p_r = p_0 \sin(\theta/2)$. By substituting this into Eq. (4.1-1), we obtain

$$\Delta r \geq \frac{h}{\Delta p_r} = \frac{h}{p_0 \sin(\theta/2)} = \frac{h}{(h/\lambda_0)\sin(\theta/2)} = \frac{\lambda_0}{\sin(\theta/2)}.$$

If the object space or the specimen space has a refractive index of n_0, we must use the fact that the wavelength in the medium is equal to λ/n_0, where λ is the wavelength in air or in vacuum. The above equation, therefore, becomes

$$\Delta r \geq \frac{\lambda}{n_0 \sin(\theta/2)} = \frac{\lambda}{NA}, \tag{4.1-2}$$

where $NA = n_0 \sin(\theta/2)$ is called the *numerical aperture*. Similarly, to find the depth of focus, Δz, we have

$$\Delta z \Delta p_z \geq h, \tag{4.1-3}$$

where Δp_z is the momentum difference between rays CA′ and CC′ along the z-direction as shown in Fig. 4.1, which is given by

$$\Delta p_z = p_0 - p_0 \cos(\theta/2).$$

By substituting this expression into Eq. (4.1-3), we have

$$\Delta z \geq \frac{h}{\Delta p_z} = \frac{h}{p_0[1 - \cos(\theta/2)]} = \frac{\lambda_0}{[1 - \cos(\theta/2)]},$$

which can be written as

$$\Delta z \geq \frac{\lambda_0}{[1 - \sqrt{1 - \sin^2(\theta/2)}]}$$

$$\approx \frac{2\lambda_0}{\sin^2(\theta/2)} = \frac{2n_0\lambda}{NA^2},$$ (4.1-4)

where we have used $\sqrt{1 - \sin^2(\theta/2)} \approx 1 - \frac{1}{2}\sin^2(\theta/2)$ by assuming $\sin^2(\theta/2) \ll 1$ in order to obtain the last expression. Now, by combining Eqs. (4.1-2) and (4.1-4), we have

$$\frac{(\Delta r)^2}{\Delta z} \geq \frac{\lambda_0}{2}.$$ (4.1-5)

This "*uncertainty relationship*" tells us that, for example, by increasing the lateral resolution by a factor of two, the depth of focus must then be decreased by a factor of four. Hence, we see that the higher the lateral resolution is, the shorter the depth of focus will be. Three-dimensional imaging in microscopy therefore aims to develop techniques that can provide high lateral resolution, and at the same time maintain a large depth of focus in order to observe a thick specimen without any difficulty.

In the past decade, we have witnessed an impressive emergence of three-dimensional (3-D) imaging techniques for microscopy. *Optical sectioning microscopy* and *scanning confocal microscopy* are the two most common techniques currently available in practice.
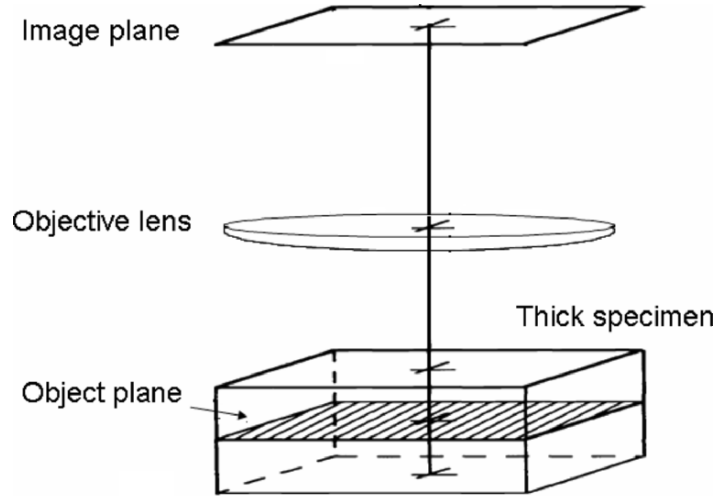
Fig. 4.2 Optical sectioning microscope (OSM).

An optical sectioning microscope (OSM), shown in Fig. 4.2, uses a wide-field microscope to sequentially record a series of images focused at different depths [Agard (1984)]. Since each 2-D image contains the in-focus as well as the out-of-focus information, reconstruction of the 3-D

information, i.e., extraction of the in-focus information from these 2-D images, is required. Many reconstruction algorithms have been developed for this purpose. However, the difficulty of optical sectioning lies in the fact that during the recording stage it is important that exact longitudinal spacing between adjacent 2-D images must be accurately controlled. Also, precise registration of the 2-D images is critical even before any computer processing can be performed.

By recognizing these problems, a radically new microscope design known as the scanning confocal microscope (SCM) has emerged [Wilson and Sheppard (1984)]. The confocal principle was first described by Minsky [Minsky, US Patent (1961)]. In scanning confocal microscopy, a doubly focused objective lens system and a pin-hole aperture in front of a photodetector are used to image only a single point within the 3-D specimen, as shown in Fig. 4.3. All the light from the point on the plane of focus (solid rays) is focused at the pin-hole aperture and passed into the photodetector. The light from the out-of-focus plane (dashed rays) is rejected by the pin-hole. Three-dimensional information is gathered by scanning the specimen in three dimensions while collecting the light transmitted through the specimen with the photodetector.
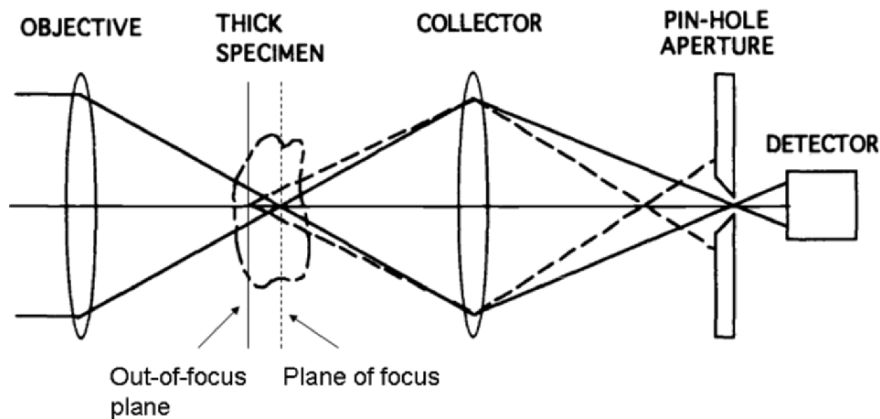

Fig. 4.3 Scanning confocal microscope (SCM).

Theoretically, SCMs provide a slightly better lateral resolution than that of OSMs. If the lateral resolution in optical sectioning microscopy is $\Delta r = \lambda/NA$, the lateral resolution of the scanning confocal microscope is $0.73\Delta r$ [Corle and Kino (1996)]. In other words, one can achieve better resolution through confocal imaging. However, such a theoretical limit has never been achieved in practice. One of the main problems associated with SCMs is that the scanning instrumental tolerances required to achieve high resolution imaging and a long working *depth of field* are very difficult to obtain in practice. The term depth of field, Δl, here refers to the range of

object (or specimen) distances that are imaged within a distance, Δz, i.e., the depth of focus in the image space. In fact, if M is the lateral magnification of the imaging system, then $\Delta l = \Delta z / M^2$ [see Example 4.1, page 112].

In essence, both methods (OSM and SCM) require precise 3-D positioning devices. This is particularly critical for the confocal methods whose technologically sophisticated and expensive equipment need special technical training to ensure proper use. However, for certain applications in biology, the main drawback of these instruments is that the data is sequentially acquired by a slow 3-D scan. This tedious data acquisition time is a serious drawback for *in vivo* studies. It precludes, for example, the possibility of monitoring dynamic interactions at the intercellular level. In addition, an extensive data acquisition time exacerbates the *photo-bleaching* problem in *fluorescence microscopy* [Pawley (1995)]. Briefly, damage caused by photo-bleaching refers to the fact that a specimen will not fluoresce when it is over-exposed. The severity of this problem in cell studies has prompted the development of extremely sophisticated techniques such as *two-photon scanning fluorescence imaging*, for example. We also want to point out that *optical coherent tomography* (OCT), which is based on interferometry, is another pertinent and emerging technique used for 3-D microscopy [Huang, Swanson, Lin, Shuman, Stinson, Chang, Hee, Flotte, Gregory, Puliafito, and Fujimoto (1991)]. But once again, this technique also requires scanning the object along the depth direction. Actually, all existing commercialized microscopes (OSM, SCM, and OCT) require axial-scanning in order to achieve 3-D imaging. Eliminating the need for a 3-D scan, or more specifically for a depth-scan gives us the impetus to study novel holographic methods for 3-D microscopy.

Holography can be used in applications where 3-D data sets are desirable but axial scanning is difficult or sometimes impossible to utilize. With holography, we have the ability to capture high resolution 3-D information in a large volume space. In recent years, holographic microscopy has become more and more prevalent because it represents a novel departure from conventional 3-D microscopy mentioned above [Zhang and Yamaguchi (1998), Kim (2000)]. Traditionally, holographic microscopy has been used in biology, however it is inherently insensitive to incoherent emissions, such as fluorescence, which makes its usefulness severely limited in life sciences applications. A scanning holographic microscope (SHM), which is based on the principle of optical scanning holography (OSH), can acquire 3-D information by only using single 2-D x-y scanning (no axial scanning is involved and hence there are reduced acquisition times for 3-D imaging). Most importantly, the SHM has the ability to image fluorescent samples, which is a breakthrough in holography since conventional holographic microscopes simply could not capture fluorescent specimens prior to the invention of optical scanning holography [Poon, Schilling, Indebetouw, and

Storrie, U.S. Patent (2000)]. In addition, the SHM will provide better theoretical transverse resolution even in comparison to a SCM. The resolution of a SHM is $0.5\Delta r$, where Δr is again the resolution of a wide field microscope [Indebetouw (2002)]. We will further elaborate on this topic in chapter 5. Note that OCT techniques are also not capable of fluorescent imaging. Hence, OSH is a very unique technique for 3-D biomedical applications.

In the spirit of keeping the scanning holographic microscope (SHM) at the same level of simplicity illustrated with the OSM and the SCM shown in Figs. 4.2 and 4.3, respectively, we show a SHM in Fig. 4.4. In principle, we need a time-dependent Fresnel zone plate (TDFZP) to two-dimensionally raster scan the thick specimen as shown in Fig. 4.4.
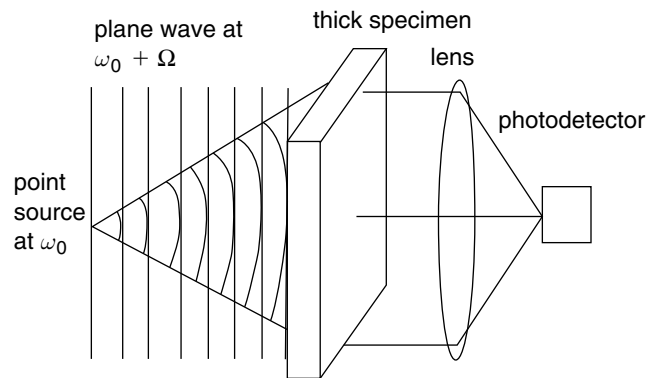

Fig. 4.4 Scanning holographic microscope (SHM).

Figure 4.5a) shows the actual setup of a scanning holographic microscope used for fluorescence applications. In this figure, two broad laser beams (originating from a 514nm-line of an argon laser), separated in temporal frequency by $\Delta\Omega$, are incident on the mirror and the beamsplitter (BS). The frequency shift in each beam is achieved by using an acousto-optic frequency shifter (AOFS). The AOFS is used in a configuration that allows us to split the laser into two beams separated in frequency by $\Delta\Omega/2\pi = 10.7$ MHz. The beams are then collimated and set parallel to each other as shown in the figure. Lens L_1 is placed in one of the beams to form the spherical wave, which is then combined collinearly with the other beam at the beamsplitter (BS). This will form a TDFZP on the object, which is at a distance of z beyond the focus of the spherical wave.

The dichroic beamsplitter transmits light at $514\,\text{nm}$ and reflects light at around 595nm. Therefore, the laser light is allowed to pass through the dichroic beamsplitter and excite the fluorescent sample, which fluoresces at 560nm. Also, the emission filter directly in front of the photomultiplier tube

(PMT) allows fluorescent light to pass through while rejecting the background laser light at 514nm. The sample is scanned through the TDFZP in a raster pattern using a computer-controlled mechanical x-y scanning platform. The current of the PMT, which contains holographic information of the scanned object, is electronically filtered, amplified at 10.7 MHz, demodulated and then digitized in synchronization with the x-y scanners in order to ultimately produce an electronic hologram. Note that the demodulation is performed by the usual electronic detection as we had previously discussed in Fig. 3.6. However, only one channel, specifically the in-phase component of the heterodyne current, was utilized during the experiment.
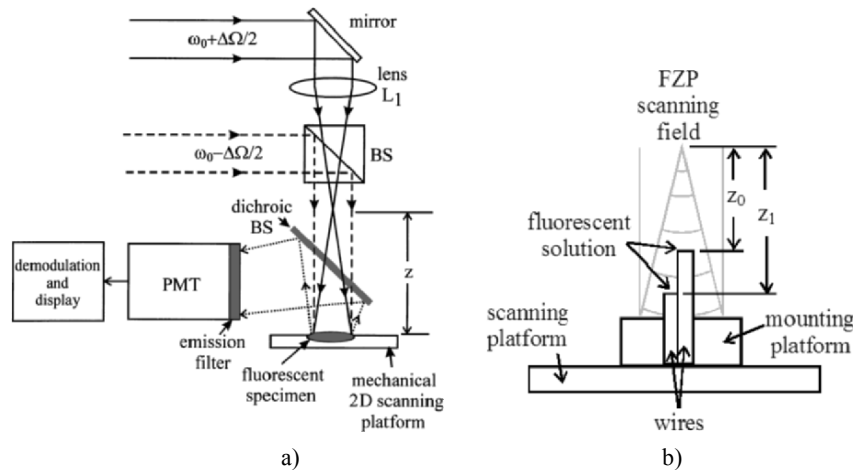

Fig. 4.5a) Experimental setup used to record the hologram of a fluorescent specimen by using OSH. PMT is a photomultiplier tube. Reprinted from B.W. Schilling et al., Optics Letters 22, 1506 (1997), with permission. © OSA. b) Experimental configuration of fluorescent solution on the ends of two wires. After Schilling (1997).

The fluorescent sample used in the experiment consists of a solution containing a high concentration of fluorescent latex beads. The beads are 15 μm in diameter and characteristically reached peak excitation at 530nm and peak emission at 560nm. To demonstrate the depth-discriminating capability of the system, we use a fluorescent object that consists of two wires adjacently placed and parallel to the optical axis but with their ends at slightly different distances from the focus of lens L1. A drop of fluorescent solution is placed on the end of each of these wires, and the two drops of solution are separated in depth by approximately 2mm (the drop on the right at $z_0 \approx 35$ mm and the drop on the left at $z_1 \approx 37$ mm, as shown in Fig. 4.5b). A hologram of this fluorescent sample was recorded and is displayed in Fig. 4.6. The two drops are easily distinguishable in the hologram.
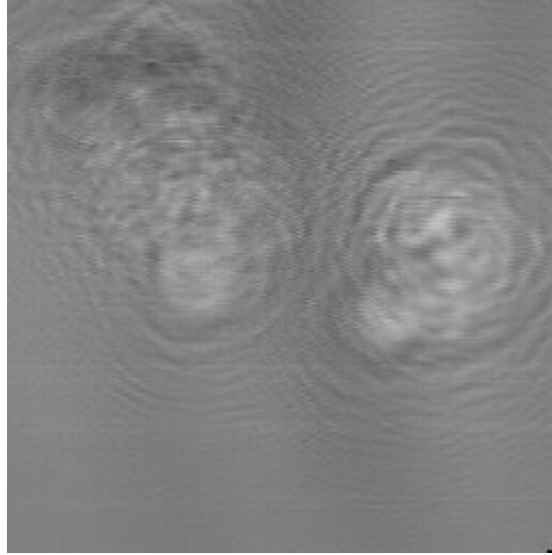
Fig. 4.6 Hologram of a fluorescent specimen recorded by using optical scanning holography. The object consists of two drops of solution containing a high concentration of fluorescent latex beads separated in depth by about 2 mm. The image is at a 256 level gray scale image consisting of 256x256 pixels. The area scanned is about 2.0 mm x 2.0 mm. Reprinted from B.W. Schilling et al., Optics Letters 22, 1506 (1997), with permission. © OSA.

The resolution of the OSH system is limited by the system's numerical aperture (NA), which actually depends on the focal length of lens L_1 ($f = 150$mm) and the diameter of the plane wave focused by lens L_1 ($D = 10$mm). The NA of the system is approximately 0.033 which corresponds to the diffraction-limited resolution limit of $\Delta r \approx 18.5 \mu$m and $\Delta z \approx 1028.4 \, \mu m$, according to Eqs. (4.1-2) and (4.1-4), respectively. The 15 μm bead size is very close to the limit that we can expect to resolve laterally with the setup.

Once the hologram has been recorded and stored, the 3-D image can then be reconstructed either optically or numerically. Numerical image reconstruction has been performed on the hologram at two different depths. Figure 4.7a) is a reconstructed image at $z_0 = 35$mm, and Fig. 4.7b) is an image reconstruction at $z_1 = 37$mm. Since the individual attributes of each fluorescent drop are not obvious in these figures, arrows are marked on the figures to indicate particular areas of interest. In Fig. 4.7a), the fluorescent drop on the left is in better focus than that on the right. The arrow in Fig. 4.7a) indicates particular beads that are more clearly visible when the hologram is reconstructed at a depth of z_0 than in Fig. 4.7b) for a depth at z_1. Similarly, the arrow in Fig. 4.7b) points out a string of four beads that are individually distinguishable when the hologram is reconstructed at a depth of z_1, but that are blurred in the image reconstruction plane z_0 in Fig. 4.7a).
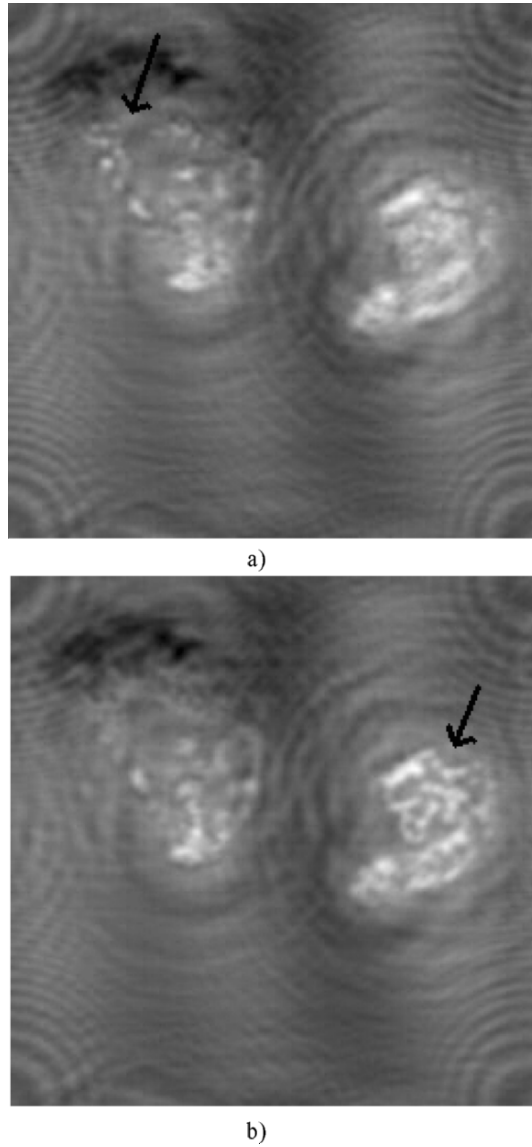
a)

b)

Fig. 4.7 Reconstruction of the hologram shown in Fig. 4.6. a) At a depth of $z_0 = 35$mm. Arrow shows individual fluorescent beads that are in focus at this depth. b) At a depth of $z_1 = 37$mm. The arrow shows four individual fluorescent beads that are in focus at this depth. Reprinted from B.W. Schilling et al., Optics Letters 22, 1506 (1997), with permission. © OSA.

Note that since only the in-phase component of the heterodyne current has been recorded to create the hologram shown in Fig. 4.6, twin-image noise (residual "fringing") exists in these reconstructions.

An important attribute of scanning holographic imaging is that this is the first time the hologram of a fluorescent specimen has been recorded by using an optical holographic technique [Poon et al., U.S. Patent (2000)]. Holography and fluorescence imaging would never seem to make conventional sense because holographic techniques require the coherent interference of light waves and fluorescence imaging does not generate coherent light. And yet, we have been able to record holograms of fluorescent specimens because optical scanning holography makes this possible. In fact, optical scanning holographic techniques can be applied to 3-D biomedical applications as fluorescence imaging [Indebetouw, Kim, Poon, and Schilling (1998)] as well as near-infared imaging [Sun and Xie (2004)] through turbid media have been demonstrated. Most recently a better than 1μm-resolution also has been established with a holographic fluorescence microscope [Indebetouw and Zhong (2006)].

4.2 Three-Dimensional Holographic TV and 3-D Display

Figure 4.8 shows a conceptual holographic system used for 3-D display with a complete recording and reconstruction stages of a point source object. As we had mentioned in chapter 2, if the recording film is replaced by, say, some electronic device such as a CCD video camera, then we can create a 3-D display by transferring the CCD's electronic output into some spatial light modulator. As we transfer the holographic information at video rate to a spatial light modulator, we create a holographic 3-D display system.

The first television transmission of a hologram was demonstrated by Enloe, Murphy, and Rubinstein [1966]. A television camera was used to record an off-axis hologram where the interference between the Fresnel diffraction pattern of an object transparency and an off-axis plane wave was recorded. The recorded hologram was then transmitted over a closed-circuit TV and displayed on a 2-D monitor. The displayed 2-D record was then photographed to form a hologram, which was subsequently reconstructed by a coherent optical system. Since then, much progress has been made and many novel devices have been invented [Macovski (1971), Brown, Noble and Markevitch, U.S. Patent (1983), Kirk, International Patent (1984), Benton (1991), Shinoda, Suzuki, Wu and Poon, U.S. Patent (1991), Schilling and Poon, U.S. Patent (2004)].
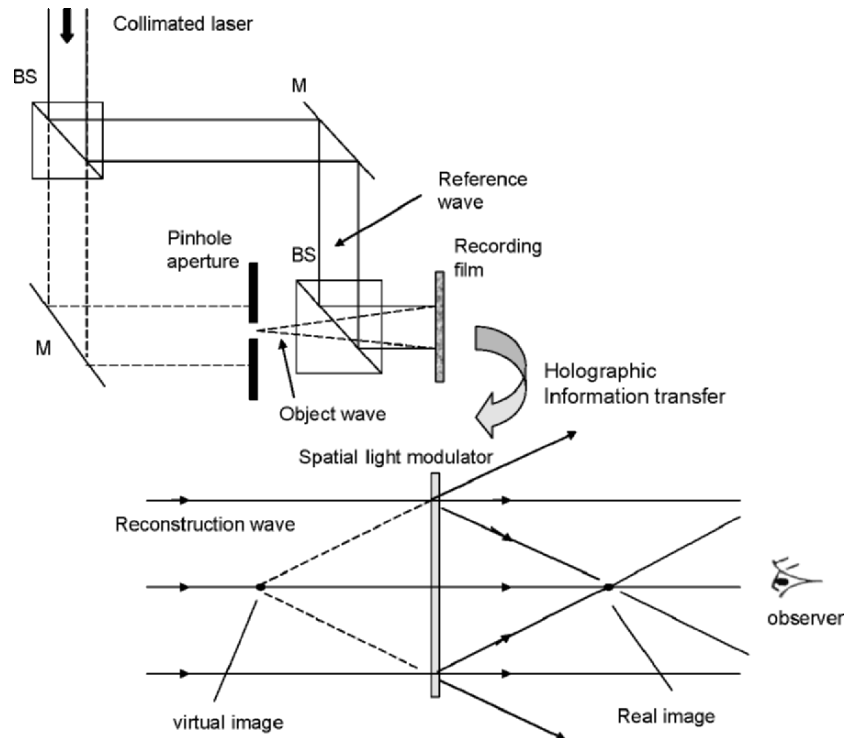
Fig. 4.8 Conceptual holographic system for 3-D display.

In this section, we will describe a recently proposed holographic TV system that uses optical scanning holography (OSH) to acquire holographic information and employs a spatial light modulator (SLM) for an eventual coherent 3-D display [Poon (2002a)]. We should be familiar with OSH by now and, therefore, we will first describe the SLM used in this system. The overall system will be subsequently discussed. The SLM, which has been experimented on the proposed TV holographic system, is called an *electron-beam-addressed spatial light modulator* (EBSLM) [Hamamatsu Photonics K.K., Japan and Hamamatsu Corp., Bridgewater, NJ]. The device is shown in Fig. 4.9.

A serial video signal is the required input to the EBSLM controller. The controller in turn provides the signal that modulates the intensity of the emission from the electron gun within the EBSLM head. This electron beam is then two-dimensionally scanned onto the surface of a $LiNbO_3$ crystal with a deflection coil. As a result, electric charges accumulate on the surface of

the crystal. The spatially induced electric field deforms the crystal as a result of the *Pockels effect* [Poon and Kim (2006)]. A pair of crossed polarizers is used in order to read the resulting spatial distribution on the crystal by laser. Conjunctly, a coherent spatial distribution of the output laser would correspond to the 2-D scanned video information on the crystal.
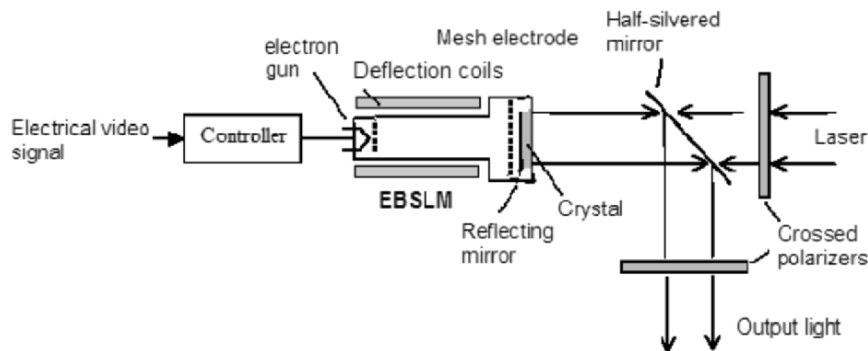

Fig. 4.9 Electron-beam-addressed spatial light modulator (EBSLM) for coherent display.

By incorporating optical scanning holography for holographic recording with EBSLM for coherent display, we can create a complete holographic TV system. This is shown in Fig. 4.10, where we have included a system for optical scanning holography on the top portion of the figure.

In the top part of the system, M1, M2, and M3 represent the mirrors, BS1 and BS2 denote the beamsplitters, AOM is an acousto-optic modulator used to shift the laser beam at a frequency of Ω, and BE1 and BE2 are the beam expanders. Note that lens L is used to focus a point source on the BS2, that projects a spherical wave through the x-y scanner to the object, while BE2 provides a plane wave onto the object. After 2-D raster scanning of the object, the photomultiplier picks up the scattered light from the object and delivers a heterodyne current as an output current. If the heterodyne current is at the radio frequency (rf) range, then it can be directly radiated through an antenna to a remote site for demodulation. At the demodulation site, we will have the usual electronic multiplexing detection. The PC can manipulate the two holograms (sine and cosine holograms) and thus deliver its output to the controller of the EBSLM for coherent reconstruction of the holographic information in order to display the output light for the audience. Hence, we have a complete holographic TV system. This system has been proposed by Poon [2002a], and this idea of using OSH to acquire holographic information and to use SLMs for display has been tested in the system shown in Fig. 4.11. It is clear from the figure that a TDFZP is used to scan the 3-D object,

and the photodetector's output is bandpass filtered at, Ω and then it is finally mixed with $\cos(\Omega t)$ to get the sine-FZP hologram, $i_c(x, y)$, as given by Eq. (3.5-3a), for coherent reconstruction by the EBSLM.
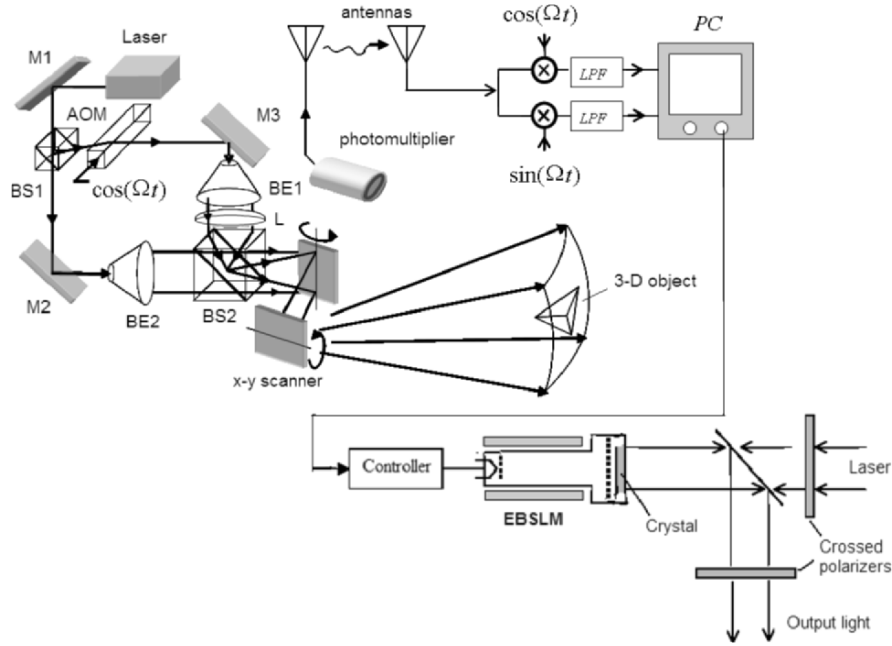

Fig. 4.10 Proposed holographic TV system. Adapted from T.-C. Poon, J. Information Display 3, 12 (2002a).

The Image Processing and Measuring System (IPMS) is a device that acts as an interface that accepts a slow-scan electrical signal and stores the information in its digital memory. The information is then converted into a NTSC video signal [Hamamatsu Photonics K.K. and Hamamatsu Corp., NJ]. When the video of the IPMS is displayed on a TV monitor, the sine-FZP hologram of a 3-D object is displayed as shown in Fig. 4.12. The 3-D object consists of two transparencies, the letters "V" and "T," located side by side but separated by a depth-distance of about 15 cm The "V" is located closer to the 2-D scanner at a distance of about 23 cm, i.e., z = 23 cm. Both letters are printed on $35mm$ film, have a line width of about 100μm, and are transmissive on an opaque background. By passing the reflected light of the EBSLM through an analyzer as shown in Fig. 4.11, a coherent image is reconstructed at a distance of $M \times$ z away from the analyzer, where z is the distance from the scanning mirror to the object (as indicated at the holographic recording stage in the figure), and M is a magnification factor

that takes into account the longitudinal magnification of the holographic imaging system that arises because of various hologram scalings. An example of the cause of *hologram scaling* may be that the displaying area of the hologram in the EBSLM is different from the actual optical scan area of the object. Holographic magnification is discussed in Example 4.1.

The reconstruction of a hologram along depth can be observed through the movable CCD camera, which focuses on different reconstruction planes. Figure 4.13a), c), and e) show the real-time reconstruction of a hologram of different depths by using the electron-beam-addressed spatial light modulator. In the 3-D reconstruction, the $M \times z$ for Fig. 4.13a) and Fig. 4.13e) are 23cm and 41cm, respectively. In Fig. 4.13a), we notice that the "V" is in focus, and in Fig. 4.13e) the "T" is now in focus. Also note that the reconstructed image planes have been contaminated by the twin-image noise because only one channel, namely the sine-FZP hologram, has been used. For comparison, we have shown digital reconstructions in Fig. 4.13b), d), and f) [Poon, Doh, Schilling, Wu, Shinoda, and Suzuki (1995)].

The EBSLM system is capable of displaying holograms at a video rate and, of course, some commercial $x - y$ scanners are also capable of working at a video rate. But what we have done is really the use of a SLM to display the acquired hologram along depth for coherent reconstruction. So what is the prospect of displaying true 3-D images in holographic television?
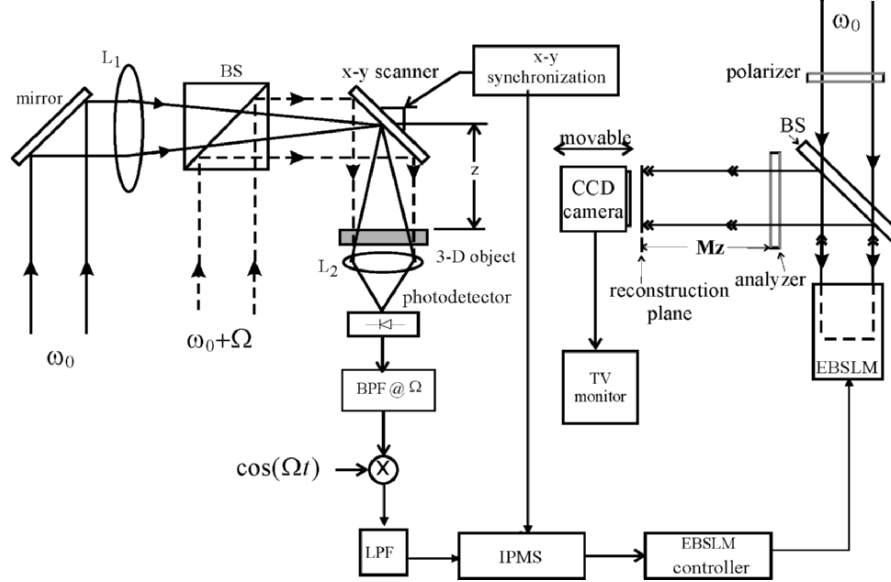

Fig. 4.11 Experimental 3-D holographic television system.
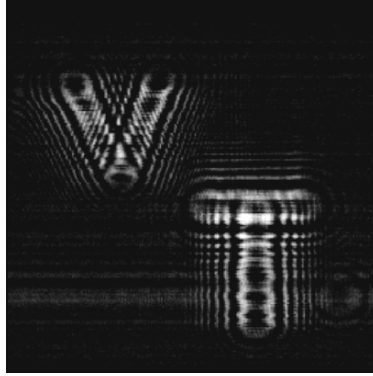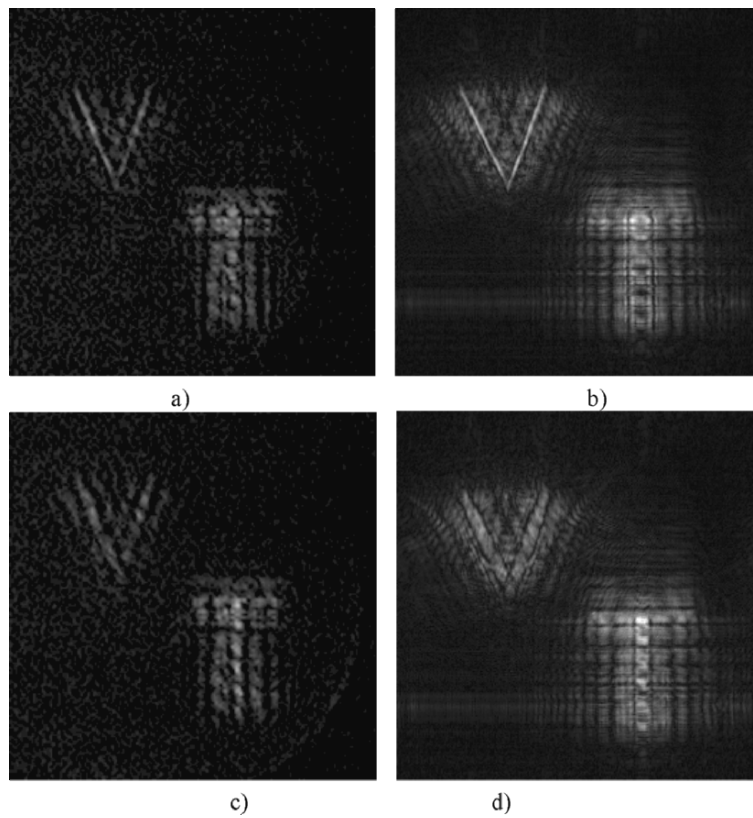Adapted from T.-C. Poon et al. Optical Review 4, 576 (1997).

Figure 4.12 Sine-FZP hologram of two letters "V" and "T" located at different depths. Reprinted from T.-C. Poon et al., Optical Engineering 34, 1338 (1995), with permission. © SPIE.

a)   b)

c)   d)

<p style="text-align:center">e)   f)</p>
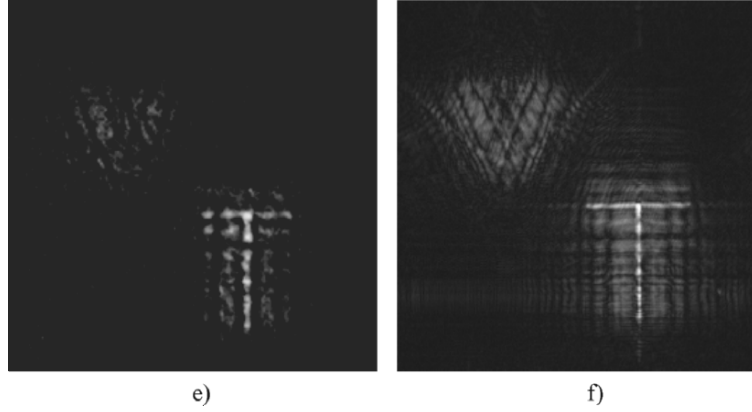
Fig. 4.13 Holographic Reconstruction. a) ,c), and e) EBSLM's reconstruction. Reprinted from
T.-C. Poon et al., Optical Review 4, 576 (1997); b), d), and f) Digital reconstruction.
Reprinted from T.-C. Poon et al., Optical Engineering 34, 1338 (1995),
with permission. © SPIE.

Example 4.1   Holographic Magnification

We will derive holographic magnification in the context of OSH. We consider a three-point object given by

$$\delta(x, y, z - z_0) + \delta(x - x_0, y, z - z_0) + \delta(x, y, z - (z_0 + \Delta z_0)), \quad (4.2\text{-}1)$$

where the first two points are located at a distance of z_0 away from the point source, which generates the spherical wave shown in Fig. 4.4. The two points have a lateral separation of x_0. The third point is located at a distance of $z_0 + \Delta z_0$ away from the first two points. According to Eq. (3.5-3a), when this three-point object is scanned, the scanned demodulated electrical signal, i_c, gives a sine-hologram, which is given by

$$H_{3\text{-}p}(x, y) \sim \; \sin[\frac{k_0}{2z_0}(x^2 + y^2)] + \sin\{\frac{k_0}{2z_0}[(x - x_0)^2 + y^2]\}$$

$$+ \sin[\frac{k_0}{2(z_0 + \Delta z_0)}(x^2 + y^2)] \; . \qquad (4.2\text{-}2)$$

If this hologram is illuminated by a plane wave at λ_0 , the three points will be reconstructed at their respective locations. We will now consider holographic magnification.

a) Hologram Scaling

Magnification can be achieved by enlarging holograms, however, it is a difficult task especially when we deal with off-axis holograms where fringe densities are of the order of several thousands lp/mm. Most photographic enlargers do not have a sufficient resolution in order to handle these details. Hence, the method is not very practical. With the scanning technique, however, on-axis holograms are generated and scaling is straightforward. The hologram can be scaled by a factor of M, simply by displaying the hologram in an area that is different from the optical scan area. In this case, Eq. (4.2-2) becomes

$$H_{3\text{-}p}(Mx, My) = \sin\{\frac{k_0}{2z_0}[(Mx)^2 + (My)^2]\}$$

$$+ \sin\{\frac{k_0}{2z_0}[(Mx - x_0)^2 + (My)^2]\}$$

$$+ \sin\{\frac{k_0}{2(z_0 + \Delta z_0)}[(Mx)^2 + (My)^2]\}. \qquad (4.2\text{-}3)$$

When $M<1$, we have magnification, whereas $M>1$ corresponds to demagnification. By re-writing Eq. (4.2-3), we have

$$H_{3\text{-}p}(Mx, My) = \sin[\frac{k_0}{2z_0/M^2}(x^2 + y^2)]$$

$$+ \sin\{\frac{k_0}{2z_0/M^2}[(x - x_0/M)^2 + y^2]\} + \sin\{\frac{k_0}{2(z_0 + \Delta z_0)/M^2}(x^2 + y^2)\}.$$

$$(4.2\text{-}4)$$

Now, during optical reconstruction using a wavelength λ_0, we see that by inspection of the first and second term in Eq. (4.2-4), the two real image points are now formed at a distance of z_0/M^2 away from the hologram, and with a reconstructed lateral distance of x_0/M away from each other. By defining the *lateral magnification*, M_{lat}, as the ratio of the reconstructed lateral distance to the original lateral distance, x_0, we have $M_{\text{lat}} = 1/M$. In order to determine the magnification along the longitudinal direction, we must focus on the first and the third terms, and upon reconstruction, we see that the two points are reconstructed at z_0/M^2 and $(z_0 + \Delta z_0)/M^2$, respectively. By defining the *longitudinal magnification*, M_{long}, as the ratio of the reconstructed longitudinal distance, $\Delta z_0/M^2$, to the original longitudinal distance, Δz_0, we have $M_{\text{long}}=1/M^2$.

b) Wavelength Scaling

We could reconstruct the hologram with a different wavelength, say $m\lambda_0$ (or k_0/m), where m is a constant. Hence, according to Fresnel diffraction, the field distribution at z away from the hologram is now given by

$$H_{3\text{-}p}(x,y) * h(x,y; z, k_0/m)$$

$$\propto \left\{ \sin[\frac{k_0}{2z_0}(x^2 + y^2)] + \sin\{\frac{k_0}{2z_0}[(x - x_0)^2 + y^2]\} \right.$$

$$\left. + \sin[\frac{k_0}{2(z_0 + \Delta z_0)}(x^2 + y^2)] \right\} * \frac{jk_0/m}{2\pi z} \exp[-\frac{jk_0/m}{2z}(x^2 + y^2)].$$

$$(4.2\text{-}5)$$

This equation suggests that there will be no magnification in the lateral direction. Along the longitudinal direction, we can inspect the results of the first and the third terms. And again when we consider real image reconstruction, the first and the second term will form an image at $z = z_0/m$. The third term gives rise to a real image at $z = (z_0 + \Delta z_0)/m$. Hence, in this case $M_{lat} = 1$, and $M_{long} = 1/m$. The reconstructed volume is either compressed or expanded by a factor of $1/m$ with the same lateral magnification. When m>1, we have compression. With visible light for recording and reconstruction, m is in the range of 0.5 to 1.8. However, when using digital reconstruction, m can be arbitrarily chosen.

c) Reconstruction combining hologram scaling and wavelength scaling

If we change the scale of the hologram and use a different wavelength for reconstruction, then the combined magnification along the lateral and longitudinal direction will be $M_{lat} = 1/M$ and $M_{long} = 1/mM^2$. Therefore, we see that the reconstructed volume, $x_0\Delta z_0/mM^3$, is different from the original volume $x_0\Delta z_0$. This creates distortion when we magnify the original 3-D object. This is a well-known result of magnification in 3-D optical imaging. In order to have a true 3-D perspective on reconstruction, when the scale change of the hologram is given by M, we let m = $1/M$ which gives us $M_{lat} = m$ and $M_{long} = m$, and therefore, we obtain $M_{lat} = M_{long}$. In other words, in order to prevent distortion in 3-D imaging, we scale the hologram by a factor M, and then the reconstructing wavelength should be $m\lambda_0$, where λ_0 is the recording wavelength and m is equal to $1/M$. This is the original idea of Gabor [1949] who first conceptualized the notion during the pre-laser era to improve upon the electron microscope. Electron microscopy was the motivational factor in the development of holography.

In order to address the prospect of a true 3-D holographic TV, we will consider some issues of 3-D holographic display.

A. Spatial frequency resolution issue

Let us first delve into the spatial frequency resolution of an SLM for 3-D display. For simplicity, we will take a point source hologram as our hologram displayed on a SLM. From previous chapters, we know that the expression of such a hologram is given by $\sin[\frac{k_0}{2z_0}(x^2 + y^2)]$. Remember that z_0 is the distance of the point source away from the recording device. The local spatial frequency along the x-direction across the hologram has been given by Eq. (2.5-5), and is defined as

$$f_{local} = \frac{1}{2\pi}\frac{d}{dx}\left(\frac{k_0}{2z_0}x^2\right) = \frac{x}{\lambda_0 z_0}. \tag{4.2-6}$$

If the size of the limiting aperture of the hologram is x_{max}, then f_{local} at x_{max} is

$$f_{max} = \frac{x_{max}}{\lambda_0 z_0}, \tag{4.2-7}$$

which is the highest spatial frequency of the hologram fringes. Now assume that the SLM has a maximum spatial resolution of f_0, and if we want to record f_{max}, then we must obey the requirement of $f_0 = f_{max}$. Now, according to the geometry shown in Fig. 4.14, the NA of the hologram is

$$\sin(\theta/2) = x_{max}/z_0 , \tag{4.2-8}$$

where θ is defined as the *viewing angle*. By using Eq. (4.2-7), Eq. (4.2-8) becomes

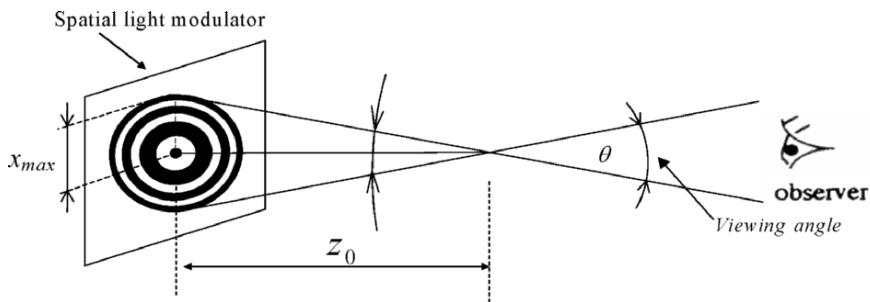$$NA = \sin(\theta/2) = \lambda_0 f_{max} = \lambda_0 f_0. \tag{4.2-9}$$

Fig. 4.14 Viewing angle.

For any given spatial resolution of the SLM, we can therefore find the viewing angle according to Eq. (4.2-9). For example, Hamamatsu's EBSLM has a spatial resolution of about $f_0 = 8$ lp/mm, which gives us a viewing angle of about 0.6° at $\lambda_0 = 0.6328\,\mu$m. Hence, such a device is not useful for applications in 3-D display. However, if we desire to obtain a sequential 2-D display along the depth, then the EBSLM system is adequate enough because it is capable of updating holograms at a video rate. Table 4.1 shows the viewing angle for some existing SLMs. We currently do not have SLMs that are suitable for 3-D display as their viewing angles are severely limited. The situation becomes even worse if we use off-axis holography because we will need to resolve the carrier frequency. As we recall, for 45 degrees of the recording angle, the carrier frequency is about 1,000 lp/mm, which is well beyond the capability of existing SLMs (see Table 4.1).

Table 4.1 Viewing angles for $\lambda_0 = 0.6328\,\mu$m.

f_0(SLM's resolution)	θ (viewing angle)	device/company
8 lp/mm	0.6 degree	EBSLM/Hamamatsu
100 lp/mm	6.8 degrees	PALSLM/Hamamatsu
500 lp/mm	34 degrees	not available

B. Spatial resolution issue

Let us calculate the number of samples that are required for a hologram to be displayed by an SLM. For a given spatial frequency resolution of an SLM, f_0, and according to the *Nyquist sampling*, the minimum sampling frequency, f_s, required in order to generate the hologram is

$$f_s = 2f_0.$$

The number of samples, N, that will then be required to create a hologram of size $l \times l$ is

$$N = (\, l f_s)^2 \;=\; (l \times 2f_0)^2 = (2l\frac{NA}{\lambda_0})^2, \qquad (4.2\text{-}10)$$

where we have used Eq. (4.2-9). According to Eq. (4.2-10), for full parallax, 20mm $\times$ 20mm on-axis hologram to be presented on an SLM, with a viewing angle of 60^0, the number of resolvable pixels required is about 1.1 billion. To put things into perspective, some of the best CCD cameras, such as Canon D60 (3072x2048 pixels, 67.7 lp/mm, 7.4 μm pixel size), have just a little over 6 Mega pixels.

C. Data transmission issue

As we had previously calculated, a single frame of a 20mm × 20mm hologram with a viewing angle of 60° requires about 1.1 billion pixels on the SLM. To update such a frame with an 8-bit resolution at 30 frames/s, a serial data rate of

1.1 billion samples/frame × 8 bits/sample × 30 frames/s = 0.26 Tbit/s

is required for full parallax.

Basically, all the issues that we have discussed illustrate the fact that content of information held within a hologram is enormous. This implies that the content of information in the hologram must be significantly reduced in order to achieve 3-D holographic TV for 3-D display. Live 3-D TV with holographic images is truly a formidable problem. However, since we are used to looking at the world with our two eyes more or less on a horizontal level, we are usually satisfied with horizontal parallax. Hence, for 512 vertical lines, the number of pixels required becomes $512 × (2l × 2NA/\lambda_0)$, which is approximately 17 million, if we are to eliminate vertical parallax. By scarifying vertical parallax, the data rate becomes 4 Gbits per second instead of 0.26 Tbits per second, which is calculated for full parallax. And this is manageable with advanced modern optical communications systems. By using fiber optics, data rates of up to 40 Gbit/s indeed can be achieved in real-world applications. The possibility of real-time holographic TV becomes a reality if the horizontal-parallax-only (HPO)-electronic holographic recording technique becomes available. Indeed, by using computer-generated, horizontal-parallax-only holographic information, the MIT group has demonstrated a 3-D holographic display having 64 vertical lines and with viewing angle of about 15 degrees [St. Hilaire, Benton, Lucente, Jepsen, Kollin, Yoshikawa, Underkoffler (1990), St. Hilaire, Benton, and Lucente (1992)]. However, this HPO-holographic information is computer generated and no HPO-holographic information has actually been generated by or recorded from actual real objects.

Optical scanning holography with horizontal-parallax-only recording is possible if we scan the object with a 1-D TDFZP. This idea, called *HPO-optical scanning holography*, has been proposed recently while computer simulations have been performed [Poon, Akin, Indebetouw, and Kim (2005), Poon (2006)].

4.3 Optical Scanning Cryptography

Due to the recent progress in the development of optical components and the increased technical performance of optical systems, optical cryptography has

a significant potential in advances for security applications. Indeed there has been a plethora of articles that deal with secure systems that use optical methods [Lohmann, Stork, and Stucke (1986), Refregier and Javidi (1995), Lai and Neifeld (2000), Wang, Sun, Su, and Chiou (2000), Magensen and Gluckstad (2001)]. One of the reasons for using optical encryption is that information, such as images, that needs to be encrypted exists already in the optical domain. Another reason is that optical encryption, as opposed to electronic or digital encryption, can provide many degrees of freedom when securing sensitive information. When large volumes of information need to be encrypted, such as a 3-D object, using optical encryption methods is probably the most logical choice. Although most optical encryption techniques are typically coherent, some incoherent optical techniques for encryption have recently been proposed [Tajahuerce, Lancis, Javidi, and Andres (2001)]. In general, incoherent optical techniques have many advantages over their coherent counterparts. This includes a better S/N ratio and insensitivity to the misalignment of optical elements. In this section, we will discuss an incoherent optical method based on optical scanning holography for encryption. This method is called *optical scanning cryptography (OSC)* [Poon, Kim, and Doh (2003)]. While having the capability to utilize incoherent processing, the method also has many other advantages. These advantages include the following. 1) Since it is an optical scanning method, it can process incoherent objects, such as printed documents, without using a spatial light modulator (SLM) to convert an incoherent image into a coherent image as existing coherent techniques currently do. The proposed system can indeed perform real-time or *on-the-fly encryption*. 2) Since the output signal is a heterodyne electrical signal, and hence the encrypted information is riding on a heterodyne frequency (or a carrier frequency as used in communications), it can immediately be radiated for wireless transmission to a secure site for storage and then subsequently be encrypted. This may have important applications in *radio frequency identification* (*RFID*) [Radio Frequency Identification Technologies: A Workshop Summary (2004)]. 3) Because the technique is based on holography, it can be easily extended to the use of encrypting 3-D information.

Figure 4.15 shows the optical system utilized for encryption and decryption. The system contains two subsystems: an encryption stage and a decryption stage. It is noted that the two subsystems have an identical two-pupil optical heterodyne scanning image processor, which we have extensively studied in section 3.4. We will first briefly summarize the previous results of the image processor, and then we will discuss encryption and decryption.
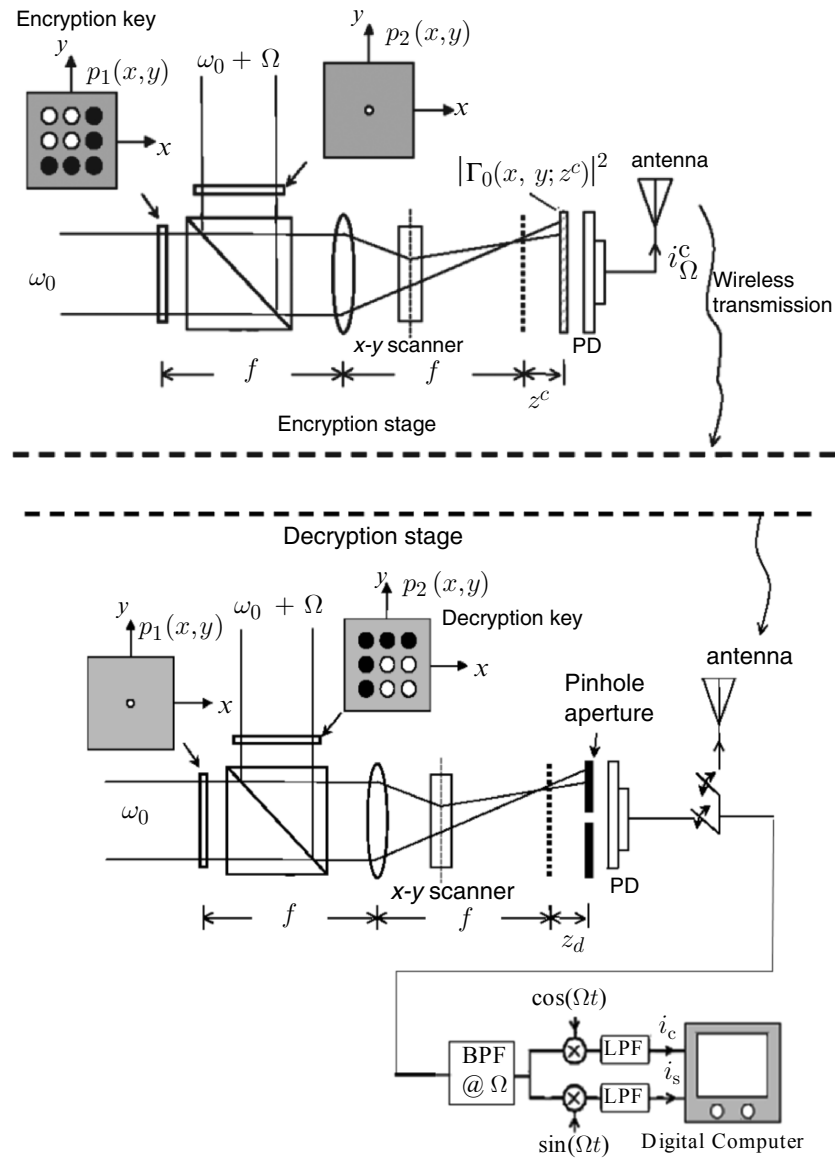
Fig. 4.15 Optical scanning cryptography.
Adapted from T.-C. Poon et al., Applied Optics 42, 496 (2003).

If we concentrate on the optical system of the encryption stage, we can see that the two pupils, $p_1(x, y)$ and $p_2(x, y)$, are located at the front focal plane of the lens and are illuminated by two broad laser beams of temporal frequencies, ω_0 and $\omega_0 + \Omega$, respectively. The two beams are then combined by a beamsplitter and used to 2-D scan a planar object, $|\Gamma_0(x, y; z^c)|^2$, located at a distance z^c away from the back focal plane of the lens. The distance of z^c is called a *coding distance*, and $|\Gamma_0(x, y; z^c)|^2$ is the object to be encrypted. The photodetector, PD, collects all the light transmitted by the object if the object is transparent (or collects all the scattered light if the object is diffusely reflecting). The photodetector will have a heterodyning current at a frequency of Ω as one of its outputs (where the other output is a baseband signal). After electronic tuning at Ω, the heterodyne current, $i_\Omega^c(x, y; z^c)$, is given by Eq. (3.4-11) where z is replaced by the coding distance z^c,

$$i_\Omega^c(x, y; z^c) = \mathrm{Re}[i_{\Omega_p}(x, y; z^c)\exp(j\Omega t)]$$

$$= \mathrm{Re}[\mathcal{F}^{-1}\{\mathcal{F}\{|\Gamma_0(x, y; z^c)|^2\}OTF_\Omega(k_x, k_y; z^c)\}\exp(j\Omega t)].$$

$$(4.3\text{-}1)$$

Again $OTF_\Omega(k_x, k_y; z^c)$ is called the optical transfer function (OTF) of the heterodyne scanning system, which has been given by Eq. (3.4-10) as follows:

$$OTF_\Omega(k_x, k_y; z^c) = \exp\left[j\frac{z^c}{2k_0}\left(k_x^2 + k_y^2\right)\right]$$

$$\times \int\int p_1^*(x', y')\, p_2(x' + \frac{f}{k_0}k_x, y' + \frac{f}{k_0}k_y)\exp\left[j\frac{z^c}{f}(x'k_x + y'k_y)\right]dx'dy',$$

$$(4.3\text{-}2)$$

where f is the focal length of the lens shown in the encryption stage in Fig. 4.15. The processing elements are the two pupil functions, $p_1(x, y)$ and $p_2(x, y)$. $i_\Omega^c(x, y; z^c)$ is the scanned and processed version of the input, $|\Gamma_0(x, y; z^c)|^2$. By manipulating the pupils, we will have a different processed output because the OTF in Eq. (4.3-2) is expressed in terms of the two pupils. Now the processed information is carried by a temporal carrier at a frequency of Ω, and if Ω is chosen to be in the radio frequency domain (which can be done easily through the use of acousto-optic modulators), then the processed information can be readily radiated to a secure site (or a decryption site) for further processing. The situation is shown in Fig. 4.15. After receiving the decrypted information from an antenna at the secure site (the output of the antenna in the secure site is switched to the input of the

bandpass filter for electronic processing), the information is further processed electronically as shown in Fig. 4.15. In other words, by multiplying the incoming signal by $\cos(\Omega t)$ and $\sin(\Omega t)$, and through lowpass filtering, we obtain two signals, i_c and i_s, respectively, which have been been given by Eqs. (3.4-14a) and (3.4-14b) as follows:

$$i_c(x, y; z^c) = \text{Re}[\mathcal{F}^{-1}\{\mathcal{F}\{|\Gamma_0(x, y; z^c)|^2\}OTF_\Omega(k_x, k_y; z^c)\}] \qquad (4.3\text{-}3a)$$

and

$$i_s(x, y; z^c) = \text{Im}[\mathcal{F}^{-1}\{\mathcal{F}\{|\Gamma_0(x, y; z^c)|^2)\}OTF_\Omega(k_x, k_y; z^c)\}]. \qquad (4.3\text{-}3b)$$

If we now apply addition to the above expressions in the following manner: $i(x, y; z^c) = i_c(x, y; z^c) + j\, i_s(x, y; z^c)$, we have a complex expression where the full amplitude and phase information of the processed object are available:

$$i(x, y; z^c) = \mathcal{F}^{-1}\{\mathcal{F}\{|\Gamma_0(x, y; z^c)|^2)\}OTF_\Omega(k_x, k_y; z^c)\}. \qquad (4.3\text{-}4)$$

Encryption

From Eq. (4.3-4), we will now discuss encryption. To perform encryption on the input object, $|\Gamma_0(x, y; z^c)|^2$, located at a distance of z^c away from the back focal plane of the lens at the encryption stage, we generally can manipulate the two pupils, $p_1(x, y)$ and $p_2(x, y)$. As a simple example, we will let $p_2(x, y) = \delta(x, y)$, a pin hole, and keep $p_1(x, y)$ as is. The situation is shown in Fig. 4.15. We shall call $p_1(x, y)$ an *encryption key*. Under these conditions, according to Eq. (4.3-2), the OTF of the system becomes

$$OTF_\Omega(k_x, k_y; z^c) = \exp\left[-j\frac{z^c}{2k_0}\left(k_x^2 + k_y^2\right)\right]p_1^*\left(\frac{-f}{k_0}k_x, \frac{-f}{k_0}k_y\right),$$

$$(4.3\text{-}5)$$

and Eq. (4.3-4) then becomes

$$i(x, y; z^c) = \mathcal{F}^{-1}\Big\{\mathcal{F}\{|\Gamma_0(x, y; z^c)|^2\}$$

$$\times \exp\left[-j\frac{z^c}{2k_0}\left(k_x^2 + k_y^2\right)\right] \times p_1^*\left(\frac{-f}{k_0}k_x, \frac{-f}{k_0}k_y\right)\Big\}. \qquad (4.3\text{-}6)$$

$i(x, y; z^c)$ is the coded or encrypted object and can be stored by the digital computer. Note that the spectrum of $|\Gamma_0(x, y; z^c)|^2$ is multiplied by two terms. Since the product of the object's spectrum with the term

$\exp\left[-j\frac{z^c}{2k_0}\left(k_x^2+k_y^2\right)\right]$ corresponds to the spectrum of the hologram of $|\Gamma_0(x,y;z^c)|^2$ [see Eq. (3.5-9)], where the object is recorded at a distance of z^c away from the focal plane of the lens, we can interpret Eq. (4.3-6) as the holographic information (or hologram) of the object that is encrypted or coded by p_1, i.e., we "encrypt the hologram of the object." This idea of coding holographic information was first investigated by Schilling and Poon in the context of optical scanning holography [Schilling and Poon (1995)].

Decryption

After the object has been coded or encrypted, it will be necessary to decode or decrypt it. To do this, we turn to the optical system at the secure site. Again, note that the optical system is the same except for the choice of the selected pupils, and the laser beams are now scanning a pin hole as an object, i.e., $|\Gamma_0(x,y;z^d)|^2 = \delta(x,y;z^d)$, located at a distance z^d away from the back focal plane of the lens at the decryption stage. We shall call z^d the *decoding distance.*

However, this time the switch, as shown in Fig. 4.15, is connected to the output of the optical system at the secure site. Through electronic processing, the output of the photodetector will then be processed. The result of Eq. (4.3-4) can be applied again, but by replacing z^c with by z^d. Now we choose $p_1(x,y) = \delta(x,y)$, a pin hole, and keep $p_2(x,y)$ as is. We shall call $p_2(x,y)$ a *decryption key*. According to Eq. (4.3-2), this selection of the pupils gives the following OTF,

$$OTF_\Omega(k_x,k_y;z^d) = \exp\left[j\frac{z^d}{2k_0}\left(k_x^2+k_y^2\right)\right]p_2(\frac{f}{k_0}k_x\,,\,\frac{f}{k_0}k_y). \qquad (4.3\text{-}7)$$

By using Eq. (4.3-4) and the fact that $\mathcal{F}\{|\Gamma_0(x,y;z^d)|^2\} = 1$, we have

$$i(x,y;z^d) = \mathcal{F}^{-1}\left\{\exp\left[j\frac{z^d}{2k_0}\left(k_x^2+k_y^2\right)\right]p_2(\frac{f}{k_0}k_x\,,\,\frac{f}{k_0}k_y)\right\}. \qquad (4.3\text{-}8)$$

This is the output generated at the decryption stage, where the decryption key has been inserted into the stage and a pin hole has been scanned. The information is now stored in the digital computer to be used to later decrypt the information coming from the encryption site via a wireless transmission. To decrypt the information represented by Eq. (4.3-6), a digital decryption unit (DDU), shown in Fig. 4.16, has been proposed.

Again, $i(x,y;z^c)$ is the transmitted encrypted information transmitted via wireless from the encryption stage, and $i(x,y;z^d)$ is the information generated at the decryption site. We see that by using Eq. (4.3-6)

and (4.3-8), at the output of the unit we have

$$\text{output of DDU} \propto \mathcal{F}^{-1}\{\mathcal{F}\{i(x,y;z^c)\} \times \mathcal{F}\{i(x,y;z^d)\}\}$$

$$= \mathcal{F}^{-1}\Big\{\mathcal{F}\{|\Gamma_0(x,y;z^c)|^2\}\exp\Big[-j\frac{z^c}{2k_0}(k_x^2+k_y^2)\Big]$$

$$\times p_1^*(\frac{-f}{k_0}k_x,\frac{-f}{k_0}k_y)\exp\Big[j\frac{z^d}{2k_0}(k_x^2+k_y^2)\Big]p_2(\frac{f}{k_0}k_x,\frac{f}{k_0}k_y)\Big\}$$

$$= |\Gamma_0(x,y;z^c)|^2 \qquad\qquad\qquad\qquad\qquad (4.3\text{-}9)$$

if the following conditions are simultaneously met. 1) $z^d = z^c$, i.e., the coding distance in the encryption stage and the decoding distance in the decryption stage are the same, and 2) $p_1^*(-x,-y)p_2(x,y) = 1$. Condition (1) simply means that the holographic reconstruction is in focus if Condition (2) has already been met. For any values of $z^d \neq z^c$, we have what is known as defocused image reconstruction. Condition (2) allows us to choose the functional form of the encryption key, $p_1(x,y)$, in the encryption stage and the decryption key, $p_2(x,y)$, at the decryption site. As a simple example, the choice of phase keys works well. We shall demonstrate this in the following example.
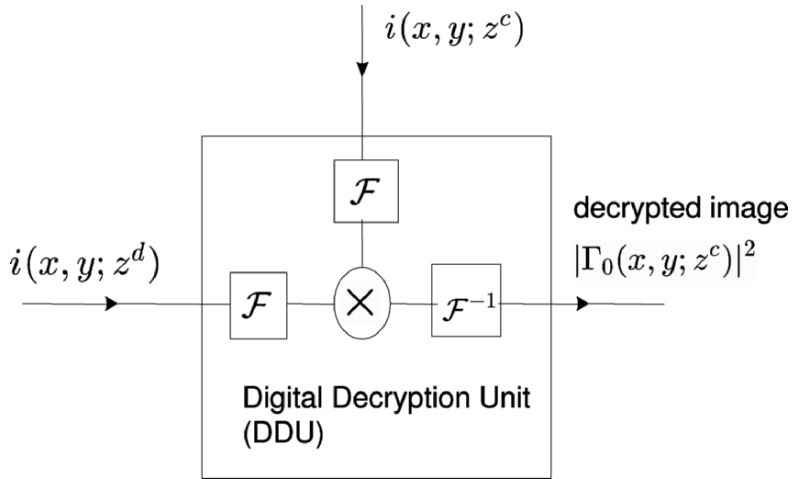

Fig. 4.16 Digital Decryption Unit (DDU) : $i(x,y;z^c)$ is the encrypted information with encryption key, $p_1(x,y)$, inserted into the encryption stage, which is sent from the encryption site via wireless transmission. $i(x,y;z^d)$ is the signal generated at the decryption site where the decryption key, $p_2(x,y)$, is inserted into the scanning stage to scan a pin hole aperture. Adapted from T.-C. Poon et el., Applied Optics 42, 496 (2003).

**Example 4.2   MATLAB Example on
Optical Scanning Cryptography**

As a simple example, we can immediately see that the choice of a random phase mask is a good encryption key, i.e., we let $p_1(x, y) = \exp[j2\pi M(x, y)]$ where $M(x, y)$ is a function of random numbers chosen from a uniform distribution between the interval (0.0,1.0). Again, $p_2(x, y) = \delta(x, y)$, i.e., a pin-hole is the other pupil in the encryption stage. For this choice of pupils, the encrypted image from Eq. (4.3-6) becomes

$$i(x, y; z^c) = \mathcal{F}^{-1}\Big\{\mathcal{F}\{|\Gamma_0(x, y; z^c)|^2\}\exp\Big[-j\frac{z^c}{2k_0}\big(k_x^2 + k_y^2\big)\Big]$$

$$\times \exp\Big[-j2\pi M(\frac{-fk_x}{k_0}, \frac{-fk_y}{k_0})\Big]\Big\}. \qquad (4.3\text{-}10)$$

The above encrypted information can be made more secure if, for example, the original document is multiplied by a random phase mask, $\exp[j2\pi r(x, y)]$, where $r(x, y)$ is a function of random numbers. By using Eq. (4.3-10), the overall encrypted image then becomes

$$i(x, y; z^c) = \mathcal{F}^{-1}\Big\{\mathcal{F}\{|\Gamma_0(x, y; z^c)|^2\exp[j2\pi r(x, y)]\}$$

$$\times \exp\Big[-j\frac{z^c}{2k_0}\big(k_x^2 + k_y^2\big)\Big]\exp\Big[-j2\pi M(\frac{-fk_x}{k_0}, \frac{-fk_y}{k_0})\Big]\Big\}.$$

$$(4.3\text{-}11)$$

This technique used to obtain the above resulting encrypted image is called *double-random phase encoding* [Refregier and Javidi (1995)]. We shall use MATLAB in order to simulate this coding. Note that $r(x, y)$ and $M(x, y)$ should be chosen as two independent random functions.

Table 4.2 contains the m-file for the simulations shown in this example. Figure 4.17a) shows the original document, $|\Gamma_0(x, y; z^c)|^2$. Figure 4.17b) and 4.17c) show the real part and imaginary part of the original document multiplied by a random phase mask, $\exp[j2\pi r(x, y)]$, placed immediately in front of the original document. Figure 4.17d) shows the "intensity" of the encrypted document, $|i(x, y; z^c)|$, which is calculated using Eq. (4.3-11) where we have used sigma = (zc*ld)/(4*pi) = (30)*(0.6*10^-6)/4π in the m-file [sigma is $z^c/2k_0$ in Eq. (4.3-11)].
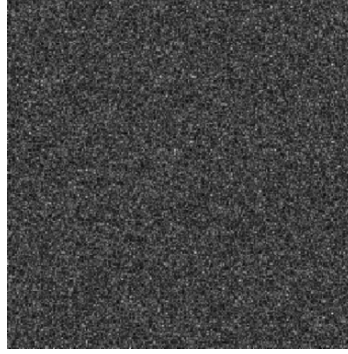
a) Original document.

b) Real part of the image multiplied by random phase mask.

c) Imaginary part of the image multiplied by random phase mask.

d) Intensity of encrypted document.

Fig. 4.17 Cryptography simulations.

For decryption, we need to gather information in the decryption stage by scanning a pin-hole object located at a distance of z^d away from the back focal plane of the lens, where the pupils are $p_1(x, y) = \delta(x, y)$ (a pin hole) and $p_2(x, y) = \exp[j2\pi M(-x, -y)]$, which satisfies Condition (2) as previously discussed. According to Eq. (4.3-8), the scanned output to be stored in the digital computer then becomes

$$i(x, y; z^d) = \mathcal{F}^{-1}\left\{\exp\left[j\frac{z^d}{2k_0}\left(k_x^2 + k_y^2\right)\right]\exp\left[j2\pi M\left(\frac{-fk_x}{k_0}, \frac{-fk_y}{k_0}\right)\right]\right\}.$$

(4.3-12)

According to Fig. 4.16, when the information from Eqs. (4.3-11) and (4.3-12) are the inputs of the DDU, the output is as follows:

$$\text{output of DDU} \propto \mathcal{F}^{-1}\left\{\mathcal{F}\{|\Gamma_0(x, y; z^c)|^2\exp[j2\pi r(x, y)]\}\right.$$

$$\times \exp\left[-j\frac{z^c}{2k_0}\left(k_x^2 + k_y^2\right)\right]\exp\left[j\frac{z^d}{2k_0}\left(k_x^2 + k_y^2\right)\right]\right\}$$

$$= |\Gamma_0(x, y; z^c)|^2\exp[j2\pi r(x, y)], \qquad (4.3-12)$$

when the sigma used in the m-file is the same as that used for encryption, i.e., theoretically $z^d = z^c$. The decrypted output intensity, i.e., the absolute value of the DDU's output, is shown in Fig. 4.18a). If the decryption key is chosen incorrectly (such as the guessing of a random phase mask), Fig. 4.18b) shows its unusable output intensity. Finally, when the decryption key is used correctly and if sigma or z^d is guessed or chosen incorrectly, say, $z^d = 1.5 \times z^c$, then the absolute value of the DDU's output is shown in Fig.
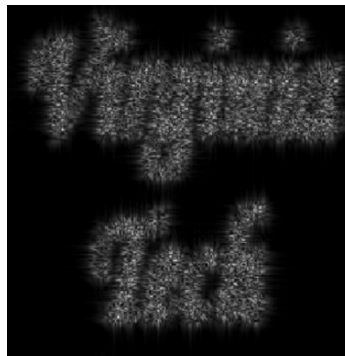
4.18c), which is a defocused version of Fig. 4.18a). We see that the introduction of z^c and z^d gives an extra security measure.

a) Intensity of decrypted document with matched key and $z^d = z^c$.
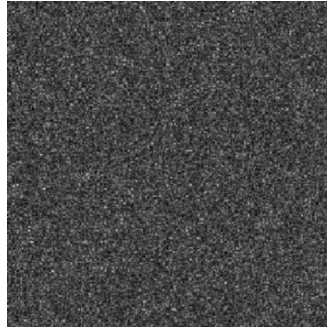
b) Intensity of decrypted document with mismatched key and $z^d = z^c$.

c) Intensity of decrypted document with matched key but with $z^d = 1.5z^c$.

Fig. 4.18 Decryption simulations.

Table 4.2 Cryptography.m:
m-file for simulating optical scanning cryptography.
- -

```
%Cryptography.m
%Simulation of Optical Encryption and Decryption
%This program was adapted from the one developed by Taegeun Kim
%of Sejong Univ., Korea

clear
%L : Normalized length of back ground (field of view)
L=1;
%Dl: Physical field of view in this simulation 20% of L
Dl=0.02;
%N : sampling number
N=255;
% dx : step size
dx=L/N;

%Unit Axis Scaling
%Normalized length and Spatial Frequency according to the Normalized length
for k=1:256
  X(k)=1/255*(k-1)-L/2;
  Y(k)=1/255*(k-1)-L/2;

  %Kx=(2*pi*k)/(N*dx)
  %k is sampling number, N is number of sample,
  %in our case, N=255, dx=1/255(unit length)

  Kx(k)=(2*pi*(k-1))/(N*dx)-((2*pi*(256-1))/(N*dx))/2;
  Ky(k)=(2*pi*(k-1))/(N*dx)-((2*pi*(256-1))/(N*dx))/2;
 end
%Real length and real spatial frequency
 X=Dl*X;
 Y=Dl*Y;
 Kx=Kx./Dl;
 Ky=Ky./Dl;

%Read Input image, image size must be 575x577x3
%for the program to function properly
CH1=imread('vt.bmp','bmp');
CH1=CH1(:,:,1);
[x,y]=meshgrid(1:577,1:575);
[xi,yi]=meshgrid(1: 2.2539:577,1:2.2461:575);
CH1p=double(CH1);
I0=interp2(x,y,CH1p,xi,yi);
I0=double(I0);
I0=I0./max(max(I0)); %Image to be encrypted

M=rand(256);
M2=rand(256);
%Encryption key in frequency domain,
```

```
%the last term in Eq. (4.3-10)
P=exp(-j*2*pi*M2);

RPM=exp(j*2*pi*M); %random phase mask, exp(j*2*pi*r(x,y))
R1=I0.*RPM;%Random phase mask times the image

%OTF(kx,ky;zc)
%sigma=z/(2Ko)=(z*ld)/(4*pi)
%where Ko is the wave number, z is the distance from the source
%and ld is the wavelength of the source
ld=0.6*10^-6; % wavelength=ld=0.6*10^-6
zc=0.3; %coding distance
sigma=(zc*ld)/(4*pi);

for r=1:256,
   for c=1:256,
  OTF(r,c)=exp(-j*sigma*(Kx(r).^2+Ky(c).^2));
   end
end

for r=1:256,
   for c=1:256,
  OTF2(r,c)=exp(-j*1.5*sigma*(Kx(r).^2+Ky(c).^2));
   end
 end

%Fourier transformation
FR=(1/256)^2*fft2(R1);
FR=fftshift(FR);
Ho=FR.*OTF;

%Encrypted image in the frequency domain
E=Ho.*P;

%Encrypted image in the space domain
e=ifft2(E); %Eq. (4.3-10)

%Key info for decryption key is achieved by scanning the pin hole that is
%located at z=zc
Key_info=conj(OTF.*P); % Fourier transform of Eq. (4.3-11),zd=zc
Key_info2=conj(OTF2.*P); % Fourier transform of Eq. (4.3-11), zd=1.5zc
%Different random phase
M3=rand(256);
P1=exp(j*2*pi*M3);
Key_info_mis=conj(OTF.*P1);% Fourier transform of Eq. (4.3-11) but with a wrong
phase key

%Decrypted image with matched key in the frequency domain
De=E.*Key_info;

%Decrypted image with matched key in the frequency domain
%but with twice distance of zc
```

```
De2=E.*Key_info2;

%Decrypted image with matched key in the space domain
de=ifft2(De); %Eq. (4.3-12)

%Decrypted image with matched key in the space domain
%but with zd=1.5 zc
de2=ifft2(De2); %Eq. (4.3-12)

%Decrypted image with mis_matched key in the frequency domain
De_mis=E.*Key_info_mis;

%Decrypted image with mis_matched key in the space domain
de_mis=ifft2(De_mis);

figure(1)
image(X,Y,256*I0);
colormap(gray(256));
axis square
title('image to be encrypted')
axis off

figure(2)
image(X,Y,255*real(R1));
colormap(gray(256));
axis square
title('Real part of the image multiplied by random phase mask')
axis off

figure(3)
image(X,Y,255*imag(R1));
colormap(gray(256));
axis square
title('Imaginary part of the image multiplied by random phase mask')
axis off

figure(4)
image(X,Y,255*abs(e)/max(max(abs(e))))
colormap(gray(256))
axis square
title('Intensity of encrypted image')% absolute value of Eq. (4.3-10)
axis off

figure(5)
image(X,Y,255*abs(de)/max(max(abs(de))));
colormap(gray(256));
axis square
title('Intensity of decrypted image with matched key with zd=zc')
axis off

figure(6)
image(X,Y,255*abs(de_mis)/max(max(abs(de_mis))));
```

```
colormap(gray(256));
axis square
title('Intensity of decrypted image with mismatched key with zd=zc')
axis off

figure(7)
image(X,Y,255*abs(de2)/max(max(abs(de2))));
colormap(gray(256));
axis square
title('Intensity of decrypted image with matched key with zd=1.5zc')
axis off
-------------------------------------------------
```

References

4.1   Agard, D. A. (1984). "Optical sectioning microscopy: cellular architecture in three dimensions," *Ann. Rev. Biophys. Bioeng.* 13, 191-219.

4.2   Benton, S.A. (1991). "Experiments in holographic video," *Proc. SPIE* IS-08, 247-267.

4.3   Brown, H. B., S.C. Noble and B.V. Markevitch (1983). Three-dimensional television system using holographic technique, *U.S. Patent # 4,376,950.*

4.4   Corle, T. R. and G. S. Kino (1996). *Confocal Scanning Optical Microscopy and Related Imaging Systems*, Academic Press, San Diego, CA.

4.5   Enloe, L. H., J.A. Murphy, and C. B. Rubinstein (1966). "Hologram transmission via television," *Bell Syst. Techn. J.* 45, 333-335.

4.6   Gabor, D. (1949). "Microscopy by reconstructed wavefronts," *Proc. Roy. Soc., ser. A*, 197, 454-487.

4.7   Hamamatsu Photonics K.K., Japan, and Hamamatsu Corp., Bridgewater, NJ. Image Processing and Measuring System (IPMS), Model DVS-3010/SS.

4.8   Hamamatsu Photonics K.K., Japan, and Hamamatsu Corp., Bridgewater, NJ. Product information sheet for EBSLM model X3636.

4.9   Huang, D., E.A. Swanson, C. P. Lin, J.S. Shuman, W.G. Stinson, W. Chang, M.R. Hee, T. Flotte, K. Gregory, C.A. Puliafito, and J. G. Fujimoto (1991). "Optical coherent tomography," *Science*, Vol. 254, 1178-1181.

4.10   Indebetouw, G. (2002). "Properties of a scanning holographic microscope: improved resolution, extended depth of focus, and/or optical sectioning," *Journal of Modern Optics* 49, 1479–1500.

4.11   Indebetouw, G., T. Kim, T.-C. Poon, and B. Schilling (1998). "Three-dimensional location of fluorescent inhomogeneities in turbid media using scanning heterodyne holography," *Optics Letters* 23, 135-137.

4.12   Indebetouw, G. and W. Zhong (2006) "Scanning holographic microscopy of three-dimensional fluorescent specimens," *Journal of the Optical Society of America* A 23, 1699-1707.

4.13   Kim, M (2000) "Tomographic three-dimensional imaging of a biological specimen using wave-scanning digital interference holography," *Optics Express* 7, 305-310.

4.14   Kim, T and T.-C. Poon (1999). "Extraction of 3-D location of matched 3-D object using power fringe-adjusted filtering and Wigner analysis," *Optical Engineering* 38, 2176-2183.

4.15   Kirk, R. L. (1984). Electronically generated holography, *International Patent* No. WO 84/00070.

4.16   Lai, S. and M. A. Neifeld (2000). "Digital wavefront reconstruction and its applications to image encryption," *Optics Communications* 178, 283-289.

4.17   Lohmann, A.W., W. Stork, and G. Stucke (1986), "Optical perfect shuffle," *Applied Optics* 25 , 1530-1531.

4.18   Macovski, A. (1971). "Considerations of television holography," *Optica Acta*, 18, 31-39.

4.19   Magensen, P.C. and J. Gluckstad (2001). "Phase-only optical decryption of a fixed mask," *Applied Optics* 8, 1226-1235.

4.20   Minsky, M. (1961). Microscopy Apparatus, *US Patent* # 3,013,467.

4.21   Pawley, J. ed. (1995). "Fundamental limits in confocal microscopy," in chapter 2 of *Handbook of Biological Confocal Microscopy*, 2nd ed., Plenum Press.

4.22   Poon, T.-C. (2002a). "Three-dimensional television using optical scanning holography," *Journal of Information Display* 3, 12-16.

4.23   Poon, T.-C. (2002b). "Optical scanning holography: principles and applications," in *Three-Dimensional Holographic Imaging*, C.J. Kuo and M. H. Tsai, ed., John Wiley & Sons, Inc.

4.24   Poon, T.-C. (2005). "Three-dimensional optical remote sensing by optical scanning holography," Current Research on Image Processing for 3D information displays, sponsored by SPIE Russia Chapter, V. Petrov, ed., *Proc. SPIE*, Vol. 5821, 41-59.

4.25   Poon, T.-C. (2006). "Horizontal-parallax-only optical scanning holography," in chapter 10 of *Digital Holography and Three-Dimensional Display: Principles and Applications*, T.-C. Poon ed., Springer, New York, USA.

4.26   Poon, T.-C, K. Doh, B. Schilling, M. Wu, K. Shinoda, and Y. Suzuki (1995). "Three-dimensional microscopy by optical scanning holography," *Optical Engineering* 34, 1338–1344.

4.27   Poon, T.-C., K. Doh, B. Schilling, K. Shinoda, Y. Suzuki, and M. Wu (1997). "Holographic three-dimensional display using an electron-beam-addressed spatial-light-modulator," *Optical Review* 567-571.

4.28   Poon, T.-C. and T. Kim (1999). "Optical image recognition of three-dimensional objects," *Applied Optics* 38, 370-381.

4.29   Poon, T.-C., B. D. Schilling, G. Indebetouw, and B. Storrie (2000). Three-dimensional holographic fluorescence microscopy, *U.S. Patent* # 6,038,041.

4.30   Poon, T.-C., T. Kim, and K. Doh (2003) "Optical scanning cryptography for secure wireless transmission," *Applied Optics* 42, 6496-6503.

4.31   Poon, T.-C., T. Akin, G. Indebetouw and T. Kim (2005). "Horizontal-parallax-only electronic holography," *Optics Express* 13, 2427-2432.

4.32   Poon, T.-C. and T. Kim (2006). *Engineering Optics with MATLAB®*, World Scientific, Singapore.

4.33   Radio Frequency Identification Technologies: A Workshop Summary (2004). *The National Academies Press*, Washington, D.C.

4.34   Refregier P. and B. Javidi (1995) "Optical image encryption using input and Fourier plane random phase encoding," *Optics Letters* 20, 767-769.

4.35   Schilling, B. W. and T.-C. Poon (1995). "Real-time pre-processing of holographic information," *Optical Engineering* 34, 3174-3180.

4.36   Schilling, B. W. (1997). "Three-dimensional fluorescence microscopy by optical scanning holography," Ph.D. dissertation, Virginia Tech.

4.37   Schilling, B., T.-C. Poon, G. Indebetouw, B. Storrie, K. Shinoda, and M. Wu (1997). "Three-dimensional holographic fluorescence microscopy," *Optics Letters* 22, 1506-1508.

4.38   Schilling, B.W. and T.-C. Poon (2004). Multicolor electronic holography and 3-D image projection system, *U.S. Patent # 6760134.*

4.39   Shinoda, K., Y. Suzuki, M. Wu and T.-C. Poon (1991). Optical heterodyne scanning type holography device, *U.S. Patent # 5064257.*

4.40   St. Hilaire, P., S. A. Benton, M. Lucente, M. Jepsen, J. Kollin, H. Yoshikawa, and J. Underkoffler (1990). "Electronic display system for computational holography," *Proc. SPIE*, vol. 1212, 174-182.

4.41   St. Hilaire, P., S. A. Benton, and M. Lucente (1992). "Synthetic aperture holography: a novel approach to three-dimensional displays," *Journal of the Optical Society of America A* 9, 1969-1977.

4.42   Sun, P and J. -H. Xie (2004). "Method for reduction of background artifacts of images in scanning holography with a Fresnel-zone-plate coded aperture," *Applied Optics* 43, 4214-4218.

4.43   Tajahuerce, E., J. Lancis, B. Javidi, and P. Andres (2001). "Optical security and encryption with totally incoherent light," *Applied Optics* 26, 678-680.

4.44   Wang, B, C.-C. Sun, W.-C. Su, and A. Chiou (2000). "Shift-tolerance property of an optical double-random phase-encoding encryption system," *Applied Optics* 39, 4788-4793.

4.45   Wilson, T. and C. Sheppard (1984). *Theory and Practice of Scanning Optical Microscopy*, Academic Press.

4.46   Zhang, T. and I. Yamaguchi (1998). "Three-dimensional microscopy with phase-shifting digital holography," *Optics Letters* 23, 1221-1223.